Korean J. Chem. Eng., 40(1), 79-90 (2023)
DOI: 10.1007/s11814-022-1312-z

pISSN: 0256-1115
eISSN: 1975-7220

Enhancement analysis of turbulent flow and heat transfer of supercritical CO_2 in a static mixer with three helical blades

Huibo Meng, Yunjuan Yao, Yanfang Yu†, Bowen Shi, and Pengcheng Ding

Engineering and Technology Research Center of Liaoning Province for Chemical Static-mixing Reaction, School of Mechanical and Power Engineering, Shenyang University of Chemical Technology, Shenyang 110142, Liaoning, P. R. China

(*Received 15 June 2022 • Revised 8 September 2022 • Accepted 5 October 2022*)

Abstract−Supercritical CO_2 has excellent flow and heat transfer characteristics, but studies are lacking on the heat transfer characteristics of static mixers using it as a working medium. To obtain the heat transfer enhancement mechanism of supercritical CO_2 within static mixers with three helical blades (TKSM), the flow and heat transfer characteristics of supercritical CO_2 in horizontal and vertically upward of TKSM were determined by three-dimensional steady-state numerical simulation at Re=7,900-22,385, respectively. With other parameters fixed, lower heat flux, inlet temperature, operating pressure, or higher mass flow corresponds to higher heat transfer coefficients (h). The orthogonal test revealed that mass flow has the greatest effect on heat transfer. Besides, the results showed that the comprehensive performance evaluation criteria (PEC) of TKSM were 1.18-1.64 times and 1.25-1.47 times of Kenics static mixer (KSM) in two different states. Considering the local deterioration of the horizontal flow, the vertically upward flow was recommended with uniform temperature distributions. Compared with the horizontal flow, the heat transfer capacity of TKSM in the upward flow increases by 92.64%-119.63%, whereas the buoyancy effect decreases by 99.83%- 99.97%.

Keywords: Static Mixer, Supercritical CO_2, Enhancement, Heat Transfer, Numerical Simulation

INTRODUCTION

The deteriorating ecological environment and energy shortages have created a dilemma of slow development for the chemical industry. Researchers have thus explored various aspects of CO_2, which is a non-toxic, non-flammable, economical, and environmentally friendly natural process gas, that has a wide range of applications in refrigeration, heat pumps, air conditioning, and various industrial fields [1-3]. Therefore, many scholars have studied the heat transfer performance of supercritical CO_2 in tubes.

Liao and Zhao [4] explored the convective heat transfer of supercritical CO_2 in vertical and horizontal microtubes with four-tube diameters. It was noticed that the buoyancy force still had a substantial effect on different flow states when Reynolds number Re exceeded 10^5. In both horizontal and vertical miniature heating tubes, the relationship for the axial average Nu of supercritical CO_2 was established. Dang and Hihara [5] investigated the heat transfer properties of supercritical CO_2 cooled in horizontal tubes with varying inner diameters by constructing an experimental platform. The heat transfer coefficient h was calculated using the modified Gnielinski equation under cooling conditions by choosing an appropriate reference temperature. Table 1 briefly summarizes investigations on the heat transfer of supercritical CO_2 flow in straight tubes [6-15], which were performed in cooling or heating conditions with diameters larger than 1 mm.

To improve the flow heat transfer performance of supercritical CO_2, many scholars have also investigated the flow heat transfer characteristics in helical tubes [16-23]. The helical tube, as an efficient heat transfer tube, has a compact structure, high heat transfer efficiency, and large utilization of unit space compared with the straight tube. Wang et al. [17] performed numerical simulations of the heat transfer of supercritical CO_2 in a heated helical tube and compared different turbulence models. The results showed that the best prediction of experimental data was provided by the shear stress transport (SST) k-ω Yang [19] performed numerical simulation of the cooling heat transfer and pressure drop characteristics of supercritical CO_2 in a horizontal helical tube and compared them with a straight tube. The results pointed out that the h and pressure drop of the helical tube were higher than those of the straight tube due to the secondary flow.

In addition to using different structures of pipes to enhance heat transfer, heat transfer efficiency could be improved by adding internal inserts in straight pipes. Many scholars have studied the heat transfer characteristics of supercritical CO_2 in a circular tube with a helical wire insert and found that the heat transfer efficiency is improved compared to that of an empty tube, and the heat transfer deterioration is delayed or suppressed under certain conditions [24-27]. As a commonly used internal insert, the static mixer is used to change the flow state by using a mixing unit fixed inside a tube to induce strong lateral mixing while suppressing axial mixing to produce good dispersion and adequate mixing between different fluids [28,29]. Due to its high productivity, safe operating conditions, low energy dissipation process, efficient mixing and heat transfer capability, it is widely applied in many fields, such as chemical and

†To whom correspondence should be addressed.
E-mail: taroyy@163.com

Table 1. Summary of studies on heat transfer characteristics of supercritical CO_2

Authors	Type	Dimensions/ mm	Operating conditions				Method	Model
			T/K	p/MPa	q/(kW/m^2)	G/(kg/s)		
Liu et al. [6]	Straight tube	D=4	/	8	15-35	0.0035	heating	Experiment SST k-ω
Zhu et al. [7]		D=4.57	/	8-10.5	12.65-50	0.0015-0.0066	heating	SST k-ω
Zhang et al. [8]		D=4-10, L=1,000	307-313	8-9	34.5-105.4	0.004-0.0125	cooling	Experiment
Yan et al. [9]		D=10, L=3,200	/	8.221/15.565	244.33-351.22	0.058-0.079	heating	SST k-ω
Bai et al. [10]		D=4, L=500	298-323	7.5-9	/	0.004-0.018	cooling	Experiment
Xiang et al. [11]		D=2/4/6, L=840	340	8	35-45	0.00126-0.0339	cooling	SST k-ω
Zhao [12]		D=22.14, L=3,653.1	288	8-9	10-20	0.48-0.72	heating	L-B low Re
Yan and Xu [13]		D=22.14, L=3,660	/	9	30-70	0.924-1.54	heating	SST k-ω
Wang et al. [14]		D=15.75/20/24.36	298-338	8-10	5-36	0.156-1.49	cooling	AKN model
Zhuang et al. [15]		D=6, L=500	800-1,050	7.5-9	100-800	0.0226-0.0565	heating	Standard k-ω
Wang et al. [16]	Helical tube	D=9, L=5,500	/	8	0-50	0-0.127	heating	Experiment
Wang et al. [17]		D=18, L=5,500	288	8	10-50	0.0995-0.305	heating	SST k-ω
Wang et al. [18]		D=4, L=560	/	8.0042-9.0072	4.20-24.3	0.00799-0.016	cooling	Experiment
Yang [19]		D=4, L=2,000	346	8-9	30	0.00754-0.0151	cooling	RNG k-ω
Liu et al. [20]		D=9, L=5,500	/	8-10	20.5-40	0.0524-0.0668	heating	SST k-ω
Liu et al. [21]		D=36, L=500	296-326	8-9	13.3-18	0.969-1.30	cooling	SST k-ω
Cheng [22]		D=9	288	8	15-25	0.0539-0.0794	heating	SST k-ω
Zhao [23]		D=100/200, L=2,281	600-660	25	50	6.28	cooling	SST k-ω

pharmaceutical industries [30,31]. The convective heat transfer characteristics of supercritical CO_2 with three different torsional ratios of twisted tape inserts (TTIs) in a heat exchanger were studied for the first time by Li et al. [32] using a three-dimensional Reynolds-average Navier-Stokes equation (RANS), energy equation, and SST turbulent flow model. The best heat transfer enhancement caused by twisted tape inserts appears at the point with two to three times better than that in water or airflow. Simões et al. [33] experimentally investigated the efficiency of Kenics static mixer in heating supercritical CO_2 in the pressure range of 8-21 MPa and established the heat transfer relationship of supercritical CO_2 about Nu according to the experimental data. Lisboa et al. [34] used different turbulence models (Standard k-ε, Reynolds Normalization Group (RNG) k-ε and Standard k-ω) to simulate the convective heat transfer efficiency of Kenics® KM static mixer preheating supercritical CO_2 at 8-20 MPa. The results showed that the RNG k-ε turbulence model was more adaptable for the simulation, and the heat transfer efficiency of the static mixer was over three-times higher than that of the smooth tube at the same heat transfer area.

According to previous research, the heat transfer and mixing performance of Newtonian and high-viscosity fluids within the KSM and related modified elements were studied [35-40]. The fluid with constant thermo-physical properties is mostly selected as the working medium for the hydrothermal performance of heat exchangers containing static mixers presently. Furthermore, supercritical CO_2 is less often considered as the working fluid in static mixers. To further investigate the effect of the static mixer on the heat transfer of supercritical CO_2, we used ANSYS Fluent v16.1 to numerically simulate the heat transfer characteristics of supercritical CO_2 in a circular tube with a static mixer with three helical blades (TKSM). The novelty of this study is to investigate the influence of TKSM on heat transfer in supercritical CO_2 flow under various working conditions, the most influential factors on heat transfer are obtained by the orthogonal test, and the heat transfer characteristics are compared with those of KSM in different flow states. This research might provide a reference for optimizing the application of a static mixer in the supercritical CO_2 heat transfer process.

The rest of the paper is organized as follows. The physical and mathematical models used in the simulations are described in the numerical methodology. In the results and discussion, the effects of heat flux, mass flow, inlet temperature and pressure are analyzed, and the influence order on heat transfer is determined using orthogonal tests. Important conclusions of this paper are listed in the final section.

NUMERICAL METHODOLOGY

1. Physical Model

The geometric model of the TKSM is shown in Fig. 1. The TKSM structure consists of three twisted helical blades with the same twist direction fixed uniformly at a circumferential angle of 120° on the shaft core, with two adjacent mixing elements oppositely twisted and staggered by 60° [40,41]. The tube diameter D is 19.1 mm and the tube length L is 1,200 mm, where the entrance and exit length of l_{in}=l_{out}=480 mm. The TKSM model employs 12 groups of mixing elements where each blade has a thickness δ of 1 mm, a length l of 20 mm, a width W of 9.55 mm (A_r=2.1), and the mixing length l_e=240 mm.

2. Mathematical Model

To evaluate the heat transfer performance of supercritical CO_2

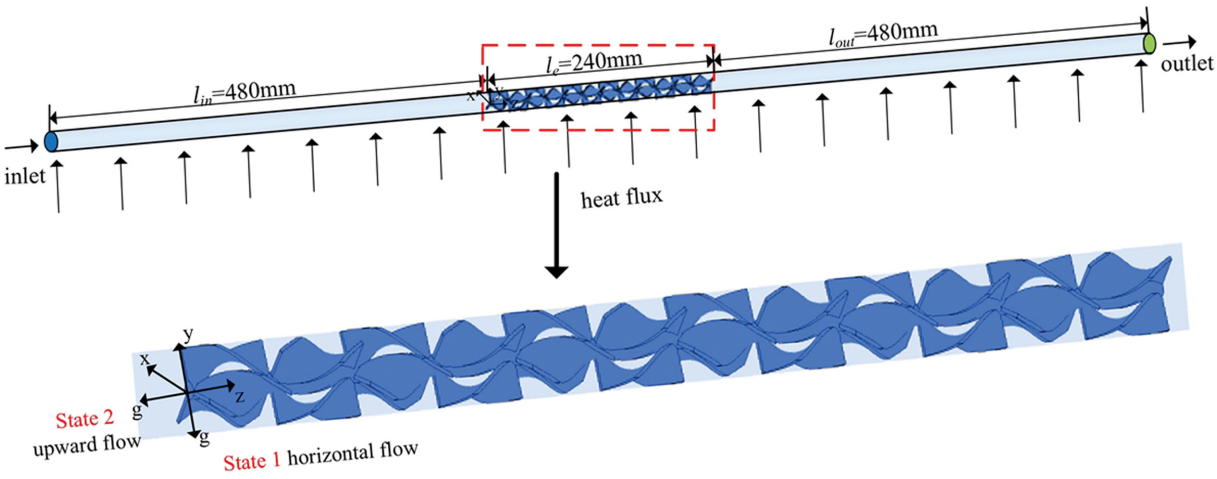

Fig. 1. Geometric model of TKSM.

inside TKSM, the following assumptions are made about the model: (1) the heat exchange between the model and the external environment during the simulation is neglected; (2) turbulence and heat transfer are conducted in the steady-state; and (3) the effect of radiation is ignored. The SST k-ω turbulence model [17] is chosen in this study. The governing equations are written as follows.

Continuity equation:

$$\frac{\partial \rho u_j}{\partial x_j} = 0 \tag{1}$$

Momentum equation:

$$\frac{\partial(\rho u_i u_j)}{\partial x_j} = \frac{\partial}{\partial x_j}\left[\mu_{eff}\left(\frac{\partial u_i}{\partial x_j}+\frac{\partial u_j}{\partial x_i}\right)-\frac{2}{3}\mu_{eff}\frac{\partial u_k}{\partial x_k}\right]+\rho g_i-\frac{\partial p_i}{\partial x_i} \tag{2}$$

Energy equation:

$$\frac{\partial(\rho u_i c_p T)}{\partial x_i} = \frac{\partial}{\partial x_i}\left[\alpha_T\left(\mu_{eff}\frac{\partial T}{\partial x_i}\right)\right]+\frac{\partial u_i}{\partial x_j}\left[\mu_{eff}\left(\frac{\partial u_i}{\partial x_j}+\frac{\partial u_j}{\partial x_i}\right)-\frac{2}{3}\mu_{eff}\frac{\partial u_k}{\partial x_k}\delta_{ij}\right] \tag{3}$$

The transport equations for turbulent kinetic energy k and specific dissipation rate ω are defined as follows [42,43]:

$$\frac{\partial}{\partial t}(\rho k)+\frac{\partial}{\partial x_i}(\rho k u_i) = \frac{\partial}{\partial x_j}\left(\Gamma_k\frac{\partial k}{\partial x_j}\right)+G_k-Y_k+S_k \tag{4}$$

$$\frac{\partial}{\partial t}(\rho \omega)+\frac{\partial}{\partial x_i}(\rho \omega u_i) = \frac{\partial}{\partial x_j}\left(\Gamma_\omega\frac{\partial \omega}{\partial x_j}\right)+G_\omega-Y_\omega+D_\omega+S_\omega \tag{5}$$

where G_k represents the generation of turbulence kinetic energy, G_ω represents the generation of ω, Γ_k and Γ_ω denote the effective diffusivity of k and ω, Y_k and Y_ω represent the dissipation of k and ω due to turbulence, D_ω represents the cross-diffusion term, S_k and S_ω are user-defined source terms.

3. Boundary Conditions and Simulation Setup

ANSYS Fluent v16.1 was used to perform the simulations. To better simulate the heat transfer characteristics of CO_2 in the supercritical state, the thermo-physical properties of CO_2 are queried using REFPROP and the thermo-physical parameters from 288 K to 330 K are input into Fluent using the Piecewise-liner method.

The Re and turbulence intensity are calculated based on the inlet empty pipe section and are defined as follows [35]:

$$Re = \frac{\rho v D}{\mu} = \frac{4G}{\pi D \mu} \tag{6}$$

$$I = 0.16 Re^{-1/8} \tag{7}$$

In the above equations, ρ, v, μ, G, and I indicate the density, the axial velocity of the inlet, the viscosity, mass flow, and the turbulence intensity, respectively.

During the simulation, the inlet is set to mass-flow-inlet and I is determined based on Eqs. (6) and (7) between Re and G. The wall and elements are set as a constant heat flux wall without slip, and the outlet is set as outflow. The operating pressure reference point is set at the outlet center to ensure the pressure throughout the computational domain. In the numerical simulation, the SIMPLE coupling algorithm is employed for pressure-velocity coupling. The least squares cell based is chosen for the gradient term. First-order upwind is adopted for momentum discretization [39], and second-order upwind is used for all other terms. The residuals of the energy equation are set to 10^{-7}, the residuals of the other equations are set to 10^{-5}, and the difference between the inlet flow and the outlet flow is less than 0.1%.

The simulation is performed under the following conditions: the mass flow G is 0.01-0.03 kg/s, which corresponds to the inlet Re in the range of 7,900-22,385, the wall heat flux q is 20-30 kW/m^2, the pressure p is 8.0-9.0 MPa and the inlet temperature T_{in} is 288-316 K.

4. Data Reduction

The local surface heat transfer coefficient h(z) is calculated by the following equation:

$$h(z) = \frac{q}{T_w(z)-T_b(z)} \tag{8}$$

The local Nusselt number Nu(z) is defined as follows:

$$Nu(z) = \frac{h(z)D}{\lambda_b(z)} \tag{9}$$

The wall temperature $T_w(z)$ is obtained from the arithmetic aver-

age of the corresponding temperatures of 12 uniformly distributed points on the wall:

$$T_w(z)=\frac{\sum_{i=1}^{12}T_{w,i}}{12} \tag{10}$$

Fluid temperature T_b could be obtained by querying enthalpy calculated by Eq. (11) and corresponding pressure in REFPROP. The formula for calculating enthalpy can be expressed as:

$$H_b(z)=H_0+\frac{q\pi Dz}{G} \tag{11}$$

where H_0 is the initial enthalpy corresponding to the inlet temperature, q is the heat flux, D is the pipe diameter, z is the distance from the starting point of the heating section to the cross-section, and G is the corresponding mass flow.

The Darcy friction factor f can be defined as follows:

$$f=\frac{2D\Delta p}{\rho v^2 L} \tag{12}$$

where Δp is the pressure drop of the tube with the measured section length L, and v is denoted the axial velocity of the inlet.

The comprehensive performance evaluation criteria (PEC) in the TKSM based on KSM under the conditions of Re=7,900-22,385 and q=25 kW/m^2 are analyzed.

$$PEC=\frac{Nu/Nu_{KSM}}{(f/f_{KSM})^{1/3}} \tag{13}$$

5. Grid Independence and Model Validation

The meshing was performed using ANSYS ICEM and Fluent meshing. Due to the large temperature gradient and velocity gradient at the near-wall location, the mesh height of the first layer is 0.01 mm with a growth rate of 1.2. The mesh quality was checked for skewness, which was below 0.770.

To verify the model grid independence, four groups of meshes were simulated under the conditions of q=25 kW/m^2, G=0.02 kg/s, T_{in}=288 K and p=8 MPa. The comparison found that the wall temperature T_w gradually stabilized as the number of grids increased as shown in Fig. 2. Table 2 lists the deviations and grid number of four meshes. The average relative deviations of T_w for the other three

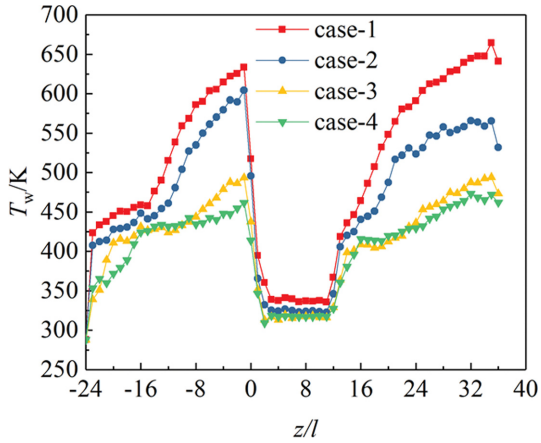

Fig. 2. Grid independence.

Table 2. Grid independence

Case	Grid number	The average relative deviation (%)
Case-1	956410	23.31
Case-2	1151623	14.24
Case-3	1345430	2.91
Case-4	1538380	-

grid models based on case-4 were 23.31%, 14.24%, and 2.91%, respectively. Therefore, the grid number of 1345430 is selected for the subsequent simulation and calculation under the consideration of calculation accuracy and operation time.

Numerical simulation of the heat transfer performance of supercritical CO_2 is important for the choice of turbulence model because its thermo-physical properties are largely influenced by temperature and pressure. To demonstrate reliability and accuracy, the experimental model of the literature [33] was chosen for the numerical simulation. The physical model was established based on the experiment and the SST k-ω turbulence model was adopted for the numerical simulation. The comparison of experimental data and numerical simulation results is shown in Fig. 3. It can be seen from Fig. 3(a) that the maximum relative error of pressure drop is 9.61% and the average error is 5.40%. From Fig. 3(b), the maximum devia-

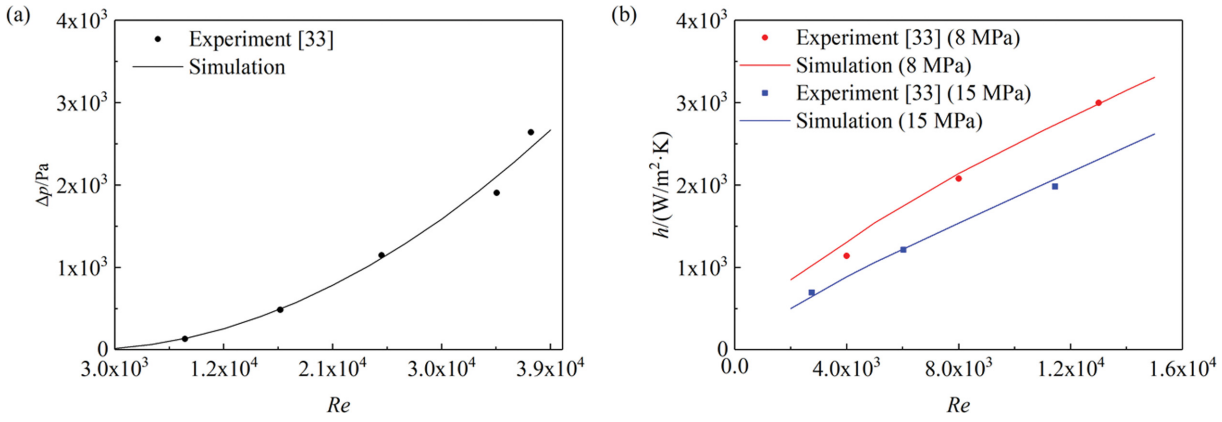

Fig. 3. Model validation.

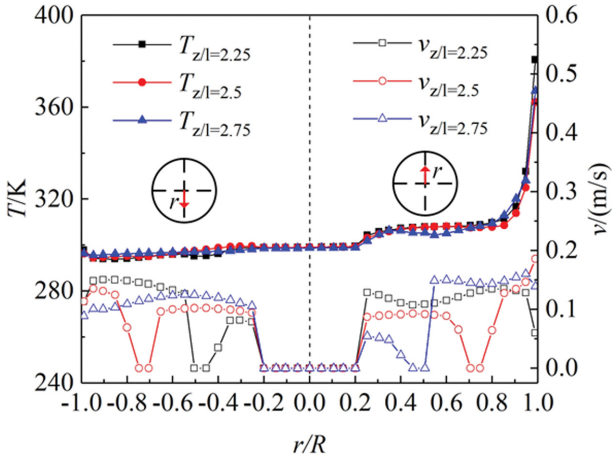

Fig. 4. Radial distribution of temperature and velocity (G=0.02 kg/s, q=25 kW/m^2, T_{in}=288 K, p=8 MPa).

tion of h at 8 MPa is 12.74%, and the average deviation is 5.1%; the maximum deviation of h at 15 MPa is 7.52%, and the average deviation is 4.36%. The numerical simulation agrees well with the experimental results, so the SST k-ω turbulence model was chosen for the subsequent simulation.

RESULTS AND DISCUSSION

1. Temperature and Velocity Distribution

To understand the variation of velocity and temperature in the supercritical CO_2 heat transfer process, the radial temperature and velocity variation curves at different positions of z/l=2.25, 2.5 and 2.75 are given in Fig. 4. It can be seen that the temperature distribution is not symmetrical along the axis, and the overall temperature at the upper wall is higher than that at the lower wall with an abrupt change occurring at 0.9<r/R<1. The lowest temperature point occurs at the bottom of the circular tube. This is because gravity is perpendicular to the direction of flow, and the fluid gathers at the bottom of the circular tube under the action of gravity so that the bottom fluid temperature is lower, and this law is verified in Fig. 5. Also, the velocity shows a clear asymmetry. In combination with Fig. 5, three vortices with the same rotation direction as the blade and a vortex radius approximately equal to the blade radius are formed around the blade. The spiral element of TKSM increases the radial mixing to prompt a significant difference between the wall temperature and the fluid temperature in the internal mixing zone. The temperature asymmetry leads to a significant difference in fluid density as well, with the low-density fluid moving upward and the high-density fluid moving downward under the action of the buoyancy force.

2. Effect of Working Conditions

The heat transfer coefficient of supercritical CO_2 was compared with different working conditions in a horizontal circular tube, and the variation is shown in Fig. 6. As shown in Fig. 6(a), the local h of CO_2 fluid increases with the increase of axial distance. The h in the non-element region changes slightly but is relatively flat; the h in the element region increases abruptly, which is about 2.34-2.46 times that in the hollow tube region. The higher the heat flux corresponds to the higher the h when z/l<−4, the change is caused by the insignificant change in physical properties when the fluid temperature is far from the proposed critical temperature range. At the same time, it is obvious that the local h is lower with the heat flux higher when z/l>6. Heat transfer is inhibited by the significant decrease of specific heat and thermal conductivity of the wall surface due to the increase of heat flux. Additionally, the more turbulent energy is suppressed and the heat transfer appears to deteriorate with the increasing heat flux, resulting in a decrease in the h [44]. For comparison, the maximum h was found to be 3,503.11 W/m^2·K for q=20 kW/m^2, which is 1.05 and 1.12 times higher than the corresponding h for q=25 and 30 kW/m^2, respectively.

In from Fig. 6(b) the h increases with increasing mass flow. Combined with Eq. (11), the higher the mass flow, the lower the corresponding fluid temperature. On the one hand, as the number of fluids reaching the critical temperature increases, the maximum value of specific heat capacity occurs at the critical state; thus the heat transfer capacity is significantly enhanced. On the other hand, the increase in CO_2 mass flow is accompanied by an increase of Re, which leads to a thinner viscous bottom layer, a thinner boundary layer, and a larger velocity gradient, thus favoring an enhanced heat transfer. The highest h for G=0.03 kg/s is 6,432.37 W/m^2·K, which is 2.55, 2.40, 1.94, and 1.44 times higher than the other conditions.

Fig. 6(c) indicates the variation of the h with the axial distance, which decreases with the increase of the inlet temperature for a given condition and decreases significantly at the inlet temperature above the pseudo-critical temperature (pseudo-critical temperature

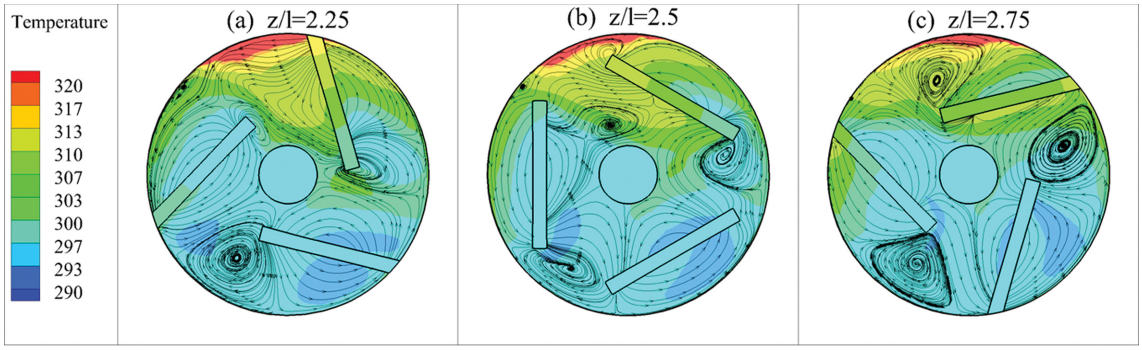

Fig. 5. Distribution of temperature and velocity fields in different cross-sections (G=0.02 kg/s, q=25 kW/m^2, T_{in}=288 K, p=8 MPa).

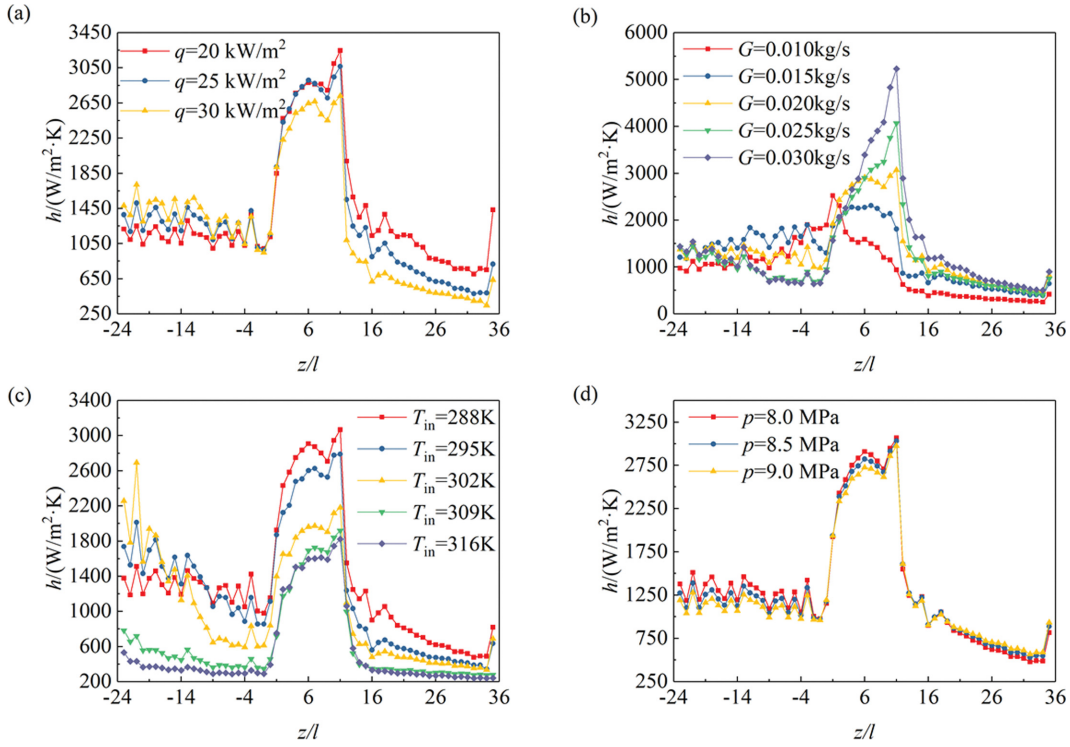

Fig. 6. Variation of heat transfer coefficient under different working conditions.

of 308 K at p=8 MPa). At a given mass flow, an increase in the inlet temperature leads to an increase in the outlet fluid temperature. This leads to the extension of the pseudo-critical region and thus poorer heat transfer performance [45]. The comparison indicates that the highest h at an inlet temperature of 302 K is 3,923.93 W/m^2·K, which is 2.04 times higher compared to 309 K.

Fig. 6(d) shows that the h of CO_2 gradually becomes smaller and the peak value gradually decreases with the increase of pressure. The reason is that the higher the pressure, the higher the wall temperature, and the temperature difference increases. Meanwhile, the specific heat capacity decreases as the pressure rises, where 8, 8.5 and 9 MPa correspond to maximum specific heat capacities of 35.27, 18.67 and 12.83 kJ/kg·K. A maximum h of 3,324.11 W/m^2·K was obtained at p=8 MPa, which is 1.01 and 1.06 times higher than the corresponding h for p=8.5 and 9 MPa. This phenomenon could be explained that the smaller the specific heat capacity, the lower the fluid temperature, and the smaller the heat transfer temperature difference, which leads to a reduction in the h.

To better evaluate the impacts of mass flow, inlet temperature, operating pressure and heat flux on heat transfer, the simulation results of the h based on the orthogonal principle are shown in Table 3. It can be seen that the main sequence affecting the heat transfer characteristics of supercritical CO_2 was obtained from the calculation results of the extreme differences: mass flow>inlet temperature>heat flux>operating pressure.

3. Effects of Buoyancy Force and Secondary Flow Intensity

For the flow in horizontal pipes, the buoyancy force parameter Gr/Re^2 is widely used, and a large number of scholars believe that the influence of buoyancy force cannot be ignored when Gr/Re^2> 10^{-3}. In this article, the effect of buoyancy force effect is characterized quantitatively through Gr/Re^2 in the fluid flow process. Meanwhile, the dimensionless number Se is introduced to characterize the change of secondary flow intensity along the flow direction, and its expression is

Table 3. Orthogonal test table of heat transfer coefficient

	G/(kg/s)	T_{in}/K	p/MPa	q/(kW/m^2)	h/(W/m^2·K)
1	0.01	288	8.0	20	123.48
2	0.01	302	8.5	25	344.29
3	0.01	316	9.0	30	190.71
4	0.02	288	8.5	30	588.80
5	0.02	302	9.0	20	447.10
6	0.02	316	8.0	25	201.18
7	0.03	288	9.0	25	704.43
8	0.03	302	8.0	30	545.90
9	0.03	316	8.5	20	258.81
R′	283.55	255.34	165.34	157.22	

$$\mathrm{Se}=\frac{\rho(\mathrm{DJ})\mathrm{D}}{\mu}=\frac{\rho\mathrm{D}^2}{\mu}\mathrm{J} \tag{14}$$

where the secondary flow J can be described as the absolute average of the vortex volume at different locations along the cross-section in the flow direction, as shown in Eq. (15) [46,47].

$$\mathrm{J}=\frac{1}{\mathrm{A}}\iint_{A}|w|\mathrm{d}A \tag{15}$$

where A is the cross-section area.

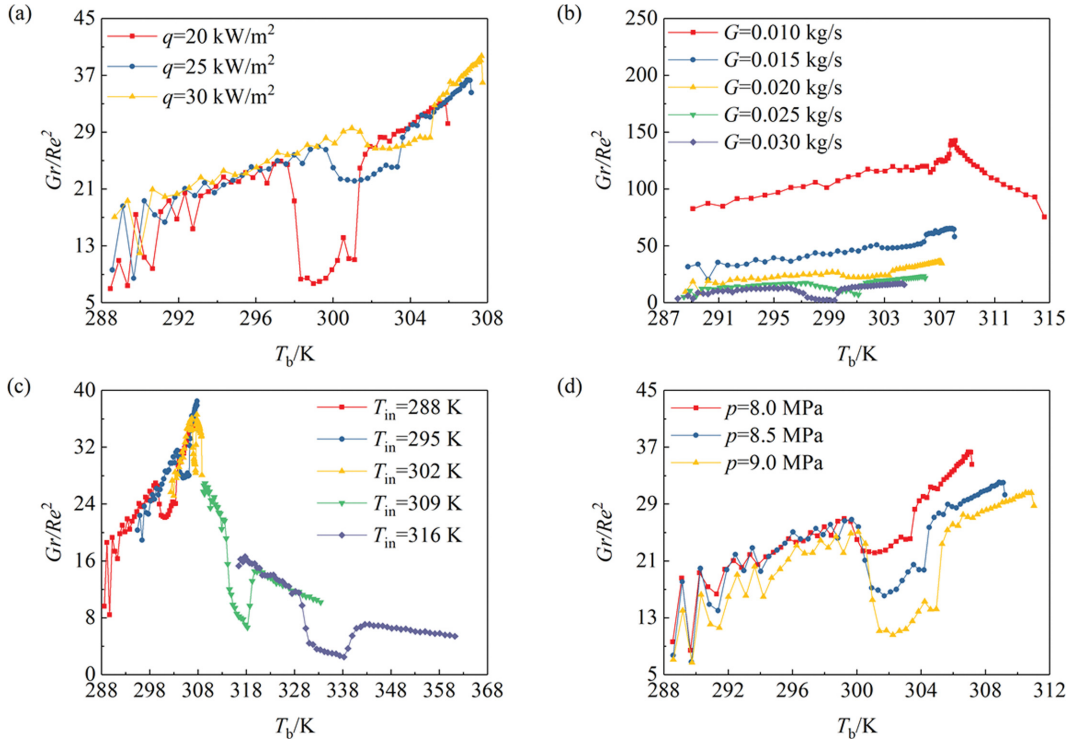

Fig. 7. Variation of Gr/Re^2 with fluid temperature for different factors.

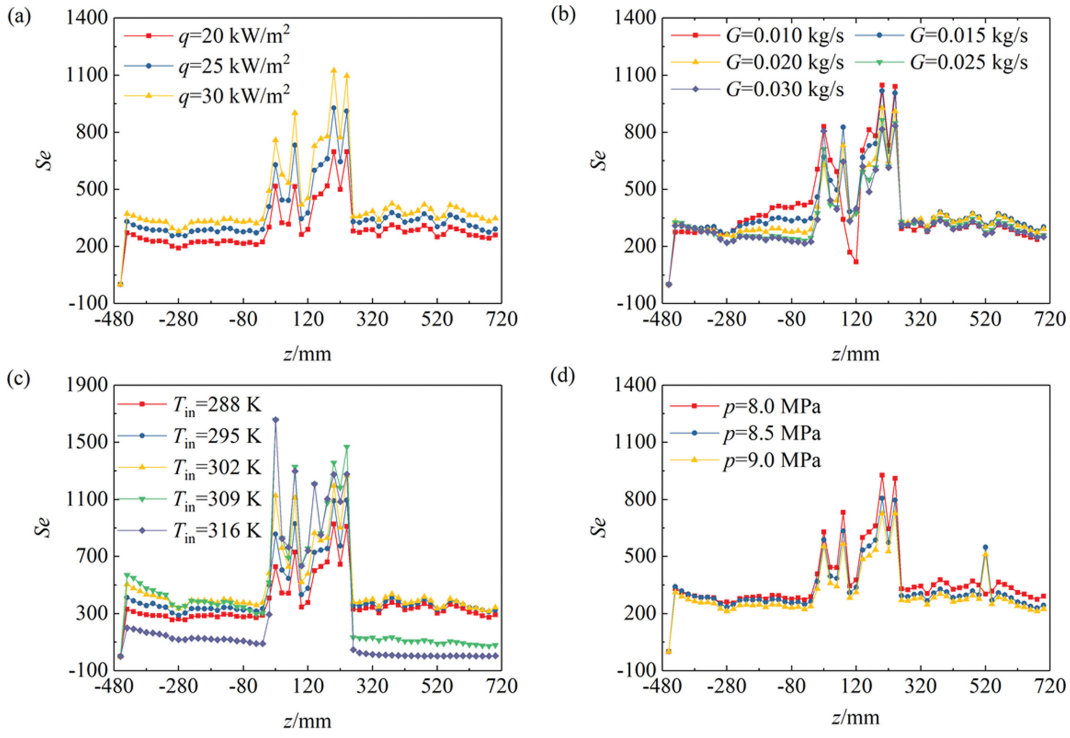

Fig. 8. Variation of Se with the axial position under different factors.

Figs. 7 and 8 depict the effects of different factors on the buoyancy force parameter and secondary flow intensity. The increase of Gr/Re^2 and Se with increasing heat flux or decreasing mass flow in the same cross-section can be seen clearly in Figs. 7(a), (b) and Figs. 8(a), (b). This could be attributed to the fact that the greater the heat flux or the smaller the mass flow, the faster the fluid temperature rises near the wall, the greater the temperature difference and the fluid density is lower. The temperature stratification becomes

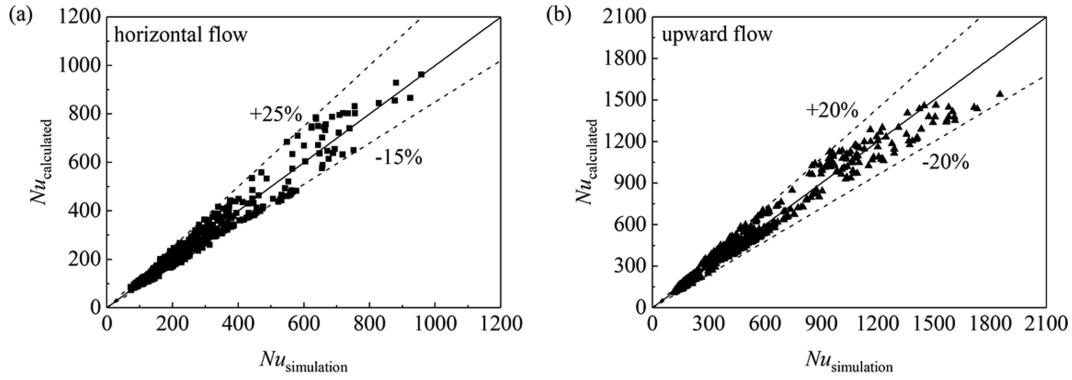

Fig. 9. Comparisons between simulated values and calculated values of fitting correlation.

more pronounced as the heat flux increases, leading to enhanced secondary flow. The fluid temperature reaches 298 K when the fluid flows through the leading edge of the first element at q= 20 kW/m^2. The temperature gradient decreases after the mixing of the elements and the temperature difference decreases, resulting in a sudden drop in buoyancy effect. The fluid temperature reaches 301 K when the fluid leaves the ending edge of the last element. The wall temperature rises rapidly, the temperature difference increases and the buoyancy effect increases dramatically. A similar trend could be seen under other operating conditions. However, as the mass flow increases, the temperature distribution gradually becomes more uniform, leading to weaker secondary flow. It is apparent in Figs. 7(c) and 8(c) that the fluid density and viscosity decrease as the temperature rises, which leads to a gradual decrease in the buoyancy effect and secondary flow intensity. As plotted in Figs. 7(d) and 8(d), the value of the buoyancy parameter and the secondary flow intensity decrease as the pressure increases, which is because the change in fluid properties begins to level off with the increasing pressure, resulting in a decrease in the buoyancy force. In summary, all the Gr/Re^2 are in the range of 2.04-142.83, which means that buoyancy effects may be evident and significant in the static mixer.

Since the significant change in the thermo-physical properties of supercritical CO_2 during the heat transfer process, in order for the changes in the thermo-physical properties of the working fluid for the effect of heat transfer could be objectively reflected, the Dittus-Boelter equation is modified by using the ratio of density and specific heat capacity, and the specific constant pressure heat capacity is replaced by the average specific heat capacity, defined as:

$$\bar{c}_p = \frac{H_w - H_b}{T_w - T_b} \tag{16}$$

where H_w and H_b denote the enthalpy of carbon dioxide corresponding to the local wall temperature and the local fluid temperature, respectively.

In the present study, multiple linear regression was used to fit the simulated data, and the following correlation equations were obtained by multiple fitting comparisons.

$$\text{for horizontal flow: } Nu = 518.92 Re^{-0.0285} Pr_b^{0.7937} \left(\frac{\rho_w}{\rho_b}\right)^{1.4231} \left(\frac{\bar{c}_p}{c_{pb}}\right)^{0.6954} \tag{17}$$

$$\text{for upward flow: } Nu = 535.55 Re^{-0.03} Pr_b^{0.961} \left(\frac{\rho_w}{\rho_b}\right)^{1.6616} \left(\frac{\bar{c}_p}{c_{pb}}\right)^{0.7556} \tag{18}$$

The new correlations of Eqs. (17) and (18) are valid for 8.0 MPa≤ p≤9.0 MPa, 288 K≤T_{in}≤316 K, 0.01 kg/s≤G≤0.03 kg/s and 20 kW/m^2≤q≤30 kW/m^2.

As can be observed from Fig. 9, the majority of data is within the upper tolerance of 25% and the lower tolerance of 15% for horizontal flow, while most are within the upper tolerance of 20% and the lower tolerance of 20% for upward flow. Cleearly, the predictive accuracy of correlations obtained under the current working conditions has high consistency with the literature [45,48].

4. Enhancement Performance of TKSM Compared with Previous Work

Figs. 10 and 11 show the temperature contour distribution of TKSM and KSM at the same cross-sections of the third element for horizontal and upward flow, respectively. Figs. 10(a)-(e) show the horizontal flow with TKSM, and (f)-(j) show the horizontal flow with KSM. Figs. 11(a)-(e) show the upward flow with TKSM, and (f)-(j) show the upward flow with KSM. In Fig. 10 the upper part of TKSM has an obvious local superheated region up to 310 K during horizontal flow, while the bottom part has an overall lower local temperature of only 295.26 K, with a difference of 14.74 K. On the other hand, KSM has an overall lower temperature and no local superheated or supercooled region, but its internal temperature distribution is not uniform, and there is a significant temperature gradient in the radial direction. Compared with the horizontal state, the internal temperature distribution of both components is more uniform in the upward flow, and no significant difference in the internal and wall temperatures was observed, as shown in Fig. 11. In general, the higher temperature gradient of the fluid occurs near the walls, while there is a lower temperature gradient in the central region. The temperature distribution of the fluid becomes uniform after passing through the elements and the temperature gradient decreases. Compared to the KSM, the TKSM has a more uniform temperature distribution and a better mixing effect. It is possible that the ability of the static mixer reduces the temperature gradient and enables a more uniform temperature distribution. The fluid is continuously guided from the center to the wall by the element, which promotes radial mixing and eliminates the temperature gradient. And the higher the number of helical blades on a section,

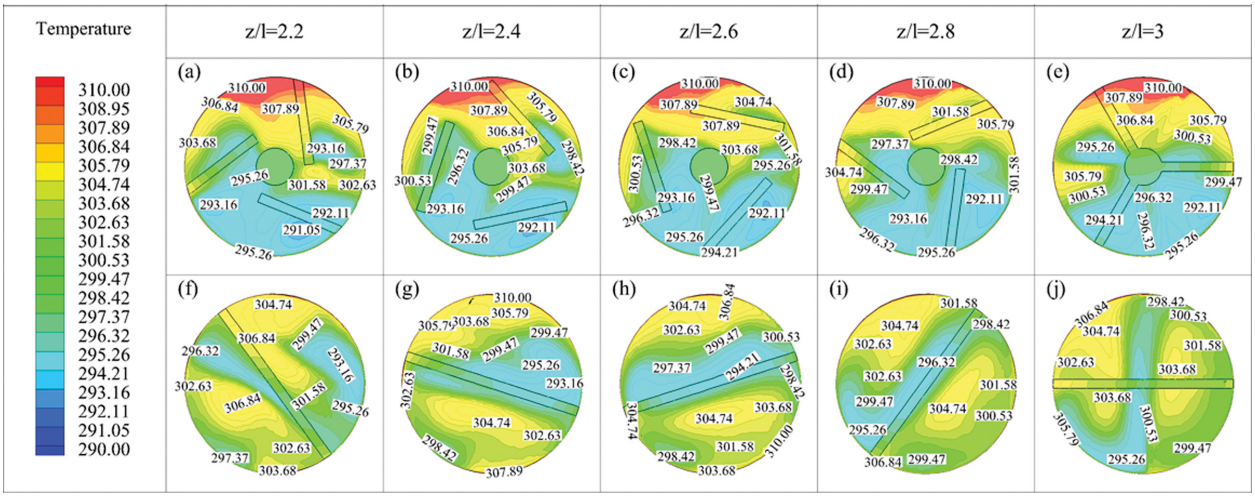

Fig. 10. Temperature contour distribution of TKSM and KSM (G=0.02 kg/s, q=25 kW/m^2, T_{in}=288 K, p=8 MPa, horizontal flow).

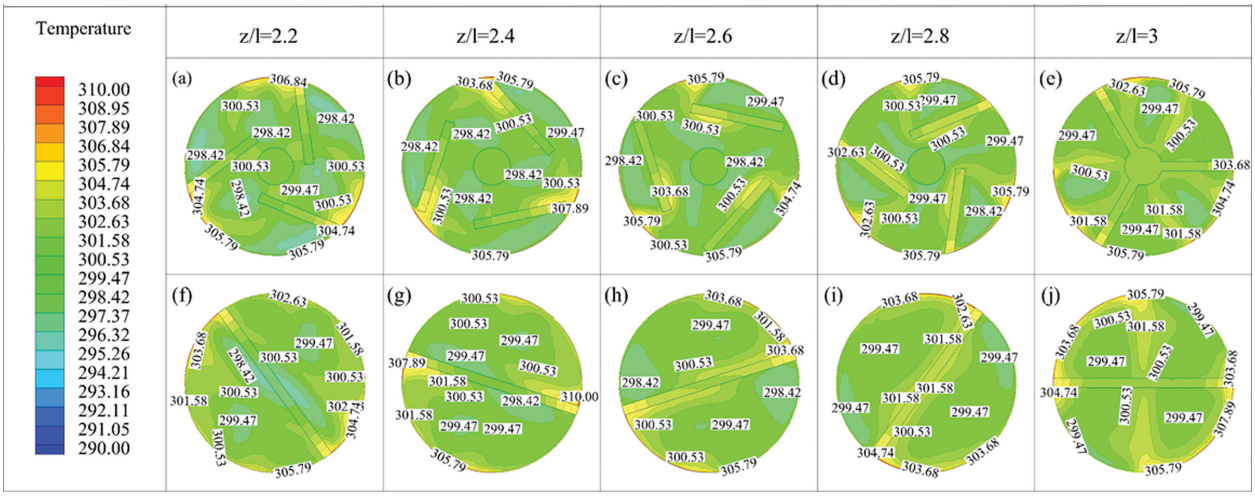

Fig. 11. Temperature contour distribution of TKSM and KSM (G=0.02 kg/s, q=25 kW/m^2, T_{in}=288 K, p=8 MPa, upward flow).

the better the radial mixing effect will be [34,49].

As shown in Fig. 12, the tube wall temperature of the mixing regions first decreases and then increases. The wall temperature of both mixers is the highest at the leading edge of the first element. In addition, the tube wall temperature of upward flow is much lower than that under horizontal flow. The average wall temperatures of TKSM in horizontal and upward flow are 314.71 K and 307.79 K, respectively. The average wall temperature of KSM in horizontal and upward flow is 310.42 K and 308.37 K, respectively. The wall temperature of the two mixers in horizontal flow is 1.02 and 1.01 times higher than those of upward flow, respectively. With the consideration of local deterioration of the horizontal static mixer as shown in Figs. 10 and 12, the vertically upward flow is recommended with uniform temperature distribution and lower wall temperature, where the wall temperature in the upward flow of TKSM and KSM are 75.41%-85.00% and 74.78%-98.77% of that in the horizontal flow under the same condition, respectively.

Fig. 13(a) shows the variation of Nu with Re for different states. The larger the Re, the higher the mass flow and the larger the Nu.

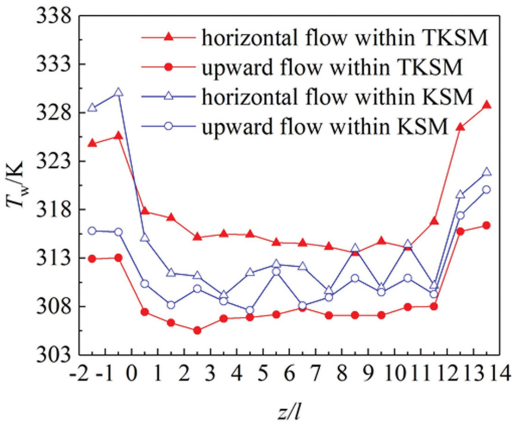

Fig. 12. Temperature changes of TKSM and KSM with axial distance (G=0.02 kg/s, q=25 kW/m^2, T_{in}=288 K, p=8 MPa).

The Nu of horizontal flow at Re>12,000 is smaller than that of upward flow. The Nu of KSM at Re=7,900 for two states is 1.18

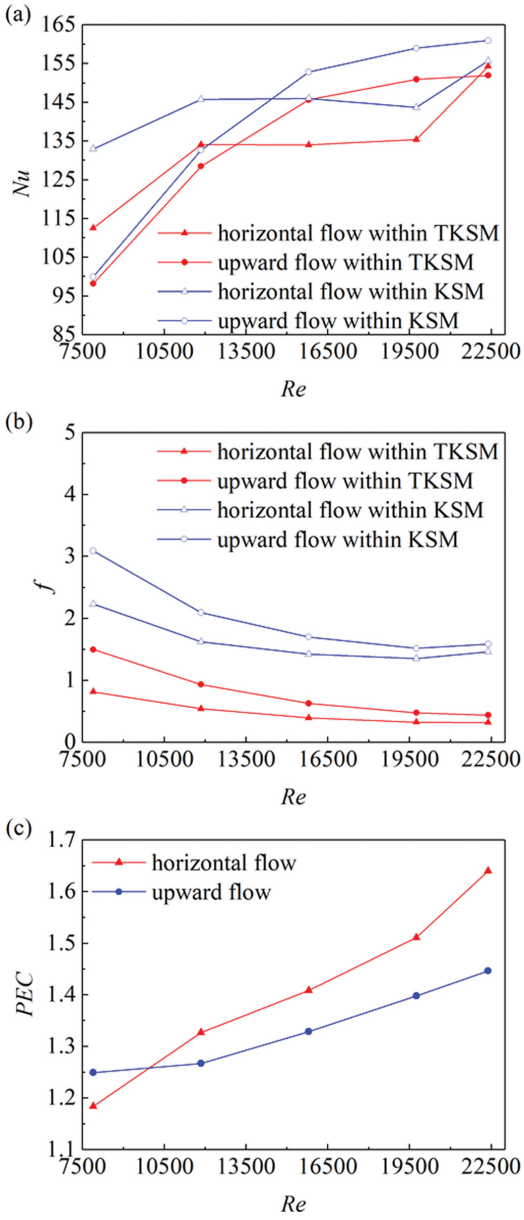

Fig. 13. The comparison of heat transfer and flow resistance between TKSM and KSM.

and 1.02 times of TKSM, and the Nu of KSM is 1.01 and 1.06 times of TKSM when Re=22385, respectively. Fig. 13(b) shows the variation of the f with Re. f decreases with increasing Re and rises slowly after Re=20,000. The pressure drop of TKSM is smaller than that of KSM under the same operating conditions [49] and the corresponding f of TKSM is 22.04%-36.49% and 27.78%-48.52% of KSM for the two states. The f of KSM is 4.54 and 3.60 times of TKSM for Re=22385, respectively. The PEC values in Fig. 13(c) become larger and larger than 1 with increasing Re. This indicates that TKSM has better heat transfer performance compared to KSM.

Based on the Filonenko correlation equation, multiple linear regression of f was performed on the basis of the simulation results combined with the variation of the thermal properties of the fluid.

for horizontal flow:

$$f=\frac{1}{(1.82\lg Re-1.64)^2}\times 14.568 Pr_b^{-0.7047}\left(\frac{\mu_w}{\mu_b}\right)^{1.5372}\left(\frac{\rho_w}{\rho_b}\right)^{-1.855} \quad (19)$$

for upward flow:

$$f=\frac{1}{(1.82\lg Re-1.64)^2}\times 15.999 Pr_b^{0.2768}\left(\frac{\mu_w}{\mu_b}\right)^{1.9869}\left(\frac{\rho_w}{\rho_b}\right)^{-1.8962} \quad (20)$$

The new correlations of Eqs. (19) and (20) are valid for 8.0 MPa≤p≤9.0 MPa, 288 K≤T_{in}≤316 K, 0.01 kg/s≤G≤0.03 kg/s and 20 kW/m^2≤q≤30 kW/m^2. As shown in Fig. 14, the calculated values are compared with the simulation results. It can be seen that the maximum error of f in the horizontal flow is less than 6.00%, as well as in the upward flow.

Fig. 15(a) shows the variation of the buoyancy effect of TKSM and KSM in horizontal and upward flow, respectively. Also, the buoyancy effect in the horizontal flow is significantly higher than that in the upward flow within the same element. The Gr/Re$^{2.7}$ corresponding to TKSM and KSM of the upward flow are 6.18×10^{-3}-3.73×10^{-2} and 6.03×10^{-3}-3.68×10^{-2}, respectively, which are only 0.03%-0.17% and 0.10%-0.20% of the horizontal flow. The buoyancy effect is gradually increased with the increasing axial distance and there is no significant difference in TKSM and KSM before the fluid arriving the first element. The Gr/Re^2 in the mixing zone and the smooth outlet section of TKSM is 98.20%-730.56% of that in KSM for horizontal flow. As a result, KSM is a good alternative for heat transfer enhancement coefficient in horizontal flow. Fig. 15(b) shows the variation of Nu with Se in two states for the

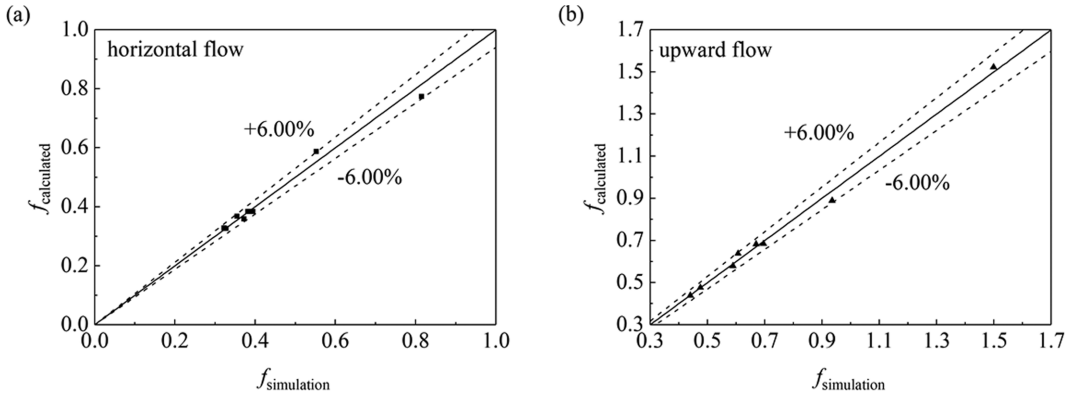

Fig. 14. Comparisons between simulated values and calculated values of f.

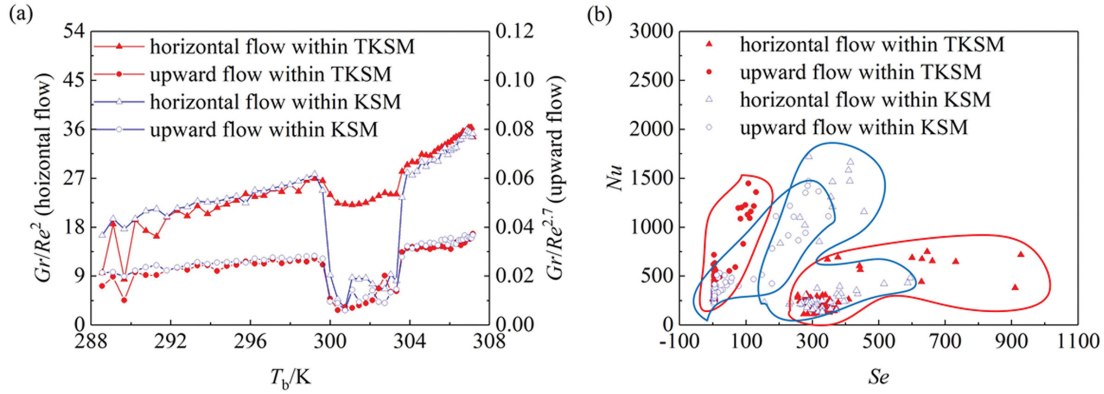

Fig. 15. Variation of buoyancy effect and Se in different states.

different mixers. The Nu values of the upward flow are larger than those of the horizontal flow, while the opposite is true for Se. The Nu and Se of the upward flow are concentrated on the left side, and those of the horizontal flow are concentrated on the lower right side. From the data in Fig. 15(b), the ranges of Se and Nu corresponding to TKSM in upward flow are 1.76-130.30 and 245.40-1448.58, respectively, which are 0.69%-14.04% and 192.64%-219.63% of the horizontal flow at the same operating conditions. The Se and Nu of the KSM in the upward flow are 2.31-348.84 and 214.16-1472.67, which are 1.49%-58.64% and 85.61%-165.87% of the horizontal flow at the same conditions. This indicates that higher Nu and better heat transfer capacity in the upward flow could be obtained with the lower Se. Also, the temperature distribution inside TKSM is more uniform in the upward flow and the average wall temperature is lower, which indicates that the heat transfer efficiency of TKSM is superior to that of KSM. Although the Nu of TKSM is slightly lower than that of KSM, the overall heat transfer performance is better because of its smaller f in the current study.

CONCLUSIONS

The heat transfer characteristics of supercritical CO_2 flow in the TKSM under horizontal and upward states were investigated numerically. The heat transfer characteristics and the effects of buoyancy force and secondary flow under different operating conditions were analyzed. Meanwhile, the heat transfer performance of the TKSM inserts was evaluated based on KSM inserts by PEC.

(1) By conducting orthogonal tests on mass flow, inlet temperature, operating pressure and heat flux, the main order of influencing the heat transfer characteristics of supercritical CO_2 was obtained as: mass flow>inlet temperature>heat flux>operating pressure.

(2) The range of the buoyancy effect of TKSM for various operating conditions in horizontal flow is 2.04-142.83, which indicates that the buoyancy effect is very significant, while the buoyancy effect of TKSM in upward flow is only 0.03%-0.17% of that in horizontal flow. The relationship equations for Nu and f are fitted by multiple linear regression, which is in good agreement with the numerical simulation values.

(3) By comparing the TKSM and KSM under the condition of horizontal and upward flow, TKSM has better comprehensive heat transfer performance. The heat transfer capacity of TKSM in upward flow is stronger by 92.64%-119.63% and the buoyancy effect is smaller by 99.83%-99.97% than that in horizontal flow, respectively. The Gr/Re^2 in the mixing zone and the smooth outlet section of TKSM is 98.20%-730.56% of that in KSM for horizontal flow. As a result, KSM is a good alternative for heat transfer enhancement coefficient in horizontal flow.

The results of the above study have some reference values for the selection of suitable static mixers for different flow states to improve the supercritical CO_2 heat transfer efficiency.

ACKNOWLEDGEMENTS

The authors acknowledge funding support for this research from the Key Scientific Research Project of Education Department of Liaoning Province (LJKZ0429), Shenyang Young and Middle-aged Science and Technology Innovation Talent Support Program (RC200032), National Natural Science Foundation of China (21476142), Distinguished Professor of Liaoning Province (LCH [2018] No. 35), the Science and Technology Research Project of Liaoning BaiQianWan Talents Program (201892151), and Natural Science Foundation of Liaoning Province (2022-MS-290, 2019-ZD-0082).

NOMENCLATURE

A_r : aspect ratio of mixing element
AKN : Abe-Kondoh-Nagano
c_p : specific heat capacity [kJ/(kg·K)]
D : diameter of the tube [mm]
G : mass flow [kg/s]
h : heat transfer coefficient [W/(m^2·K)]
H : enthalpy [kJ/kg]
I : turbulence intensity
L : length of the tub [mm]
l : length of a single mixing element [mm]
L-B : Lam-Bremhorst
Nu : Nusselt number
Δp : pressure drop [Pa]
p : pressure [MPa]
Pr : Prandtl number
q : heat flux [kW/m^2]

Re : Reynolds number
r : radial distance [mm]
R : radius [mm]
R′ : the extreme difference in the orthogonal test
RNG : Reynolds normalization group
SST : shear stress transport
T : temperature [K]
v : the axial velocity [m/s]
W : width of the element [mm]
z : distance from the starting point of the heating section to the cross-section [m]

Subscripts
b : mainstream fluid
e : element
in : inlet
out : outlet
w : wall

Greek Symbols
λ : thermal conductivity of fluid [W/(m·K)]
μ : dynamic viscosity of fluid [Pa·s]
ρ : the density of the fluid [kg/m^3]
δ : the thickness of the element [mm]

REFERENCES

1. A. Zendehboudi, Z. L. Ye, A. Hafner, T. Andresenc and G. Skaugen, *Int. J. Heat Mass Transfer*, **178**, 121641 (2021).
2. M. M. Ehsan, Z. Guan and A. Y. Klimenko, *Renew. Sust. Energ. Rev.*, **92**, 658 (2018).
3. Y. T. Ge, S. A. Tassou, I. Dewa Santosa and K. Tsamos, *Appl. Energ.*, **160**, 973 (2015).
4. S. M. Liao and T. S. Zhao, *Int. J. Heat Mass Transfer*, **45**, 5025 (2002).
5. C. B. Dang and E. Hihara, *Int. J. Refrig.*, **27**, 736 (2004).
6. X. X. Liu, X. X. Xu, C. Liu, S. J. Zhang, J. C. He and C. B. Dang, *Appl. Therm. Eng.*, **181**, 115987 (2020).
7. X. J. Zhu, R. Z. Zhang, X. Yu, M. G. Cao and Y. X. Ren, *Energies*, **13**, 3502 (2020).
8. G. W. Zhang, P. Hu, L. X. Chen and M. H. Liu, *Appl. Therm. Eng.*, **143**, 1101 (2018).
9. C. S. Yan, J. L. Xu, B. G. Zhu and G. L. Liu, *Materials*, **13**, 723 (2020).
10. W. J. Bai, X. X. Xu and Y. Y. Wu, *CIESC J.*, **67**, 1244 (2016).
11. M. R. Xiang, J. F. Guo, X. L. Huai, K. Y. Cheng, X. Y. Cui, Z. Zhang and J. Zhang, *J. Eng. Thermophy-rus.*, **38**, 1929 (2017).
12. Z. H. Zhao, Shandong Univ. (2019).
13. C. S. Yan and J. L. Xu, *Acta Phys. Sin.*, **69**, 136 (2020).
14. J. Y. Wang, Z. Q. Guan, H. Gurgenci, A. Veeraragavan, X. Kang and K. Hooman, *Int. J. Therm. Sci.*, **138**, 190 (2019).
15. X. R. Zhuang, X. H. Xu, Z. Yang, Y. X. Zhao and P. Yu, *Acta Phys. Sin.*, **70**, 176 (2021).
16. S. X. Wang, W. Zhang, Z. Y. Niu and J. L. Xu, *CIECS J.*, **64**, 3917 (2013).
17. K. Z. Wang, X. X. Xu, Y. Y. Wu, C. Liu and C. B. Dang, *J. Supercrit. Fluids*, **99**, 112 (2015).
18. K. Z. Wang, X. X. Xu, C. Liu, W. J. Bai and C. B. Dang, *Int. J. Heat Mass Transfer*, **108**, 1645 (2017).
19. M. Yang, *Appl. Therm. Eng.*, **109**, 685 (2016).
20. X. X. Liu, H. Shan, S. J. Zhang, X. X. Xu and C. Liu, *J. Eng. Thermophys-rus.*, **41**, 55 (2020).
21. X. X. Liu, J. Ye, X. X. Xu, C. Liu, K. Z. Wang, H. R. Li and W. J. Bai, *CIESC J.*, **67**, 120 (2016).
22. H. J. Zhao, X. W. Li and X. X. Wu, *J. Supercrit. Fluids*, **127**, 48 (2017).
23. J. Cheng, North China Electric Power Univ. (2020).
24. V. B. Ankudinov and V. A. Kurganov, *High Temp.*, **19**, 870 (1981).
25. B. S. Shiralkar and G. Peter, *J. Heat Transfer*, **91**, 27 (1969).
26. Z. Wang, R. Xu, C. Xiong and P. Jiang, *J. Tsinghua Univ. (Sci. & Technol.)*, **58**, 1101 (2018).
27. Y. Y. Bae, H. Y. Kim and T. H. Yoo, *Int. J. Heat Fluid Flow*, **32**, 340 (2011).
28. M. Regner, K. Östergren and C. TräGåRdh, *Chem. Eng. Sci.*, **61**, 6133 (2006).
29. S. Casey Jones, F. Sotiropoulos and A. Amirtharajah, *J. Environ. Eng.*, **128**, 5 (2015).
30. A. Ghanem, T. Lemenand, D. D. Valle and H. Peerhossaini, *Chem. Eng. Res. Des.*, **92**, 205 (2014).
31. R. K. Thakur, Ch. Vial, K. D. P. Nigam, E. B. Nauman and G. Djelveh, *Chem. Eng. Res. Des.*, **81**, 787 (2003).
32. W. G. Li, Z. B. Yu, Y. Wang and Y. L. Li, *Therm. Sci. Eng. Progress*, **31**, 101285 (2022).
33. P. C. Simões, B. Afonso, J. Fernandes and J. P. B. Mota, *J. Supercrit. Fluids*, **43**, 477 (2008).
34. P. F. Lisboa, J. Fernandes, P. C. Simões, J. P. B. Mota and E. Saatdjian, *J. Supercrit. Fluids*, **55**, 107 (2010).
35. H. B. Meng, F. Wang, Y. F. Yu, M. Y. Song and J. H. Wu, *Ind. Eng. Chem. Res.*, **53**, 4084 (2014).
36. H. B. Meng, M. Y. Song, Y. F. Yu, F. Wang and J. H. Wu, *Can. J. Chem. Eng.*, **93**, 1849 (2015).
37. H. B. Meng, G. X. Zhu, Y. F. Yu, Z. Y. Wang and J. H. Wu, *Int. J. Heat Mass Transfer*, **99**, 647 (2016).
38. H. B. Meng, M. Q. Han, Y. F. Yu, Z. Y. Wang and J. H. Wu, *Int. J. Heat Mass Transfer*, **156**, 119788 (2020).
39. H. B. Meng, J. B. Wang, Y. F. Yu, Z. Y. Wang and J. H. Wu, *Chin. J. Process Eng.*, **22**, 338 (2022).
40. H. B. Meng, Y. N. Hao, Y. F. Yu, Z. G. Li, S. N. Song and J. H. Wu, *Korean J. Chem. Eng.*, **37**, 1859 (2020).
41. J. H. Wu, Chinese Patent, 200,510,045,606.8 (2007).
42. F. R. Menter, *AIAA J.*, **32**, 1598 (1994).
43. H. B. Meng, T. Meng, Y. F. Yu, Z. Y. Wang and J. H. Wu, *Int. J. Heat Mass Transfer*, **194**, 123006 (2022).
44. D. M. McEltigot and J. D. Jackson, *Nucl. Eng. Des.*, **232**, 327 (2004).
45. L. Wang, Y. C. Pan, J. D. Lee, Y. Wang, B. R. Fu and C. Pan, *Int. J. Heat Mass Transfer*, **159**, 120136 (2020).
46. Z. M. Lin, D. L. Sun and L. B. Wang, *Heat Mass Transfer*, **45**, 1351 (2009).
47. K. W. Song and L. B. Wang, *Prog. Comput. Fluid Dyn.*, **8**, 496 (2008).
48. B. G. Zhu, X. M. Wu, L. Zhang, E. H. Sun, H. S. Zhang and J. L. Xu, *CIECS J.*, **70**, 1282 (2019).
49. B. Gong, J. Zhang, C. M. Zhang and J. H. Wu, *J. Beijing University Chem. Technol.*, **35**, 84 (2008).